ARTICLES
https://doi.org/10.1038/s41567-021-01395-w

nature physics

Check for updates

Precision mass measurement of lightweight self-conjugate nucleus ^{80}Zr

A. Hamaker[1,2,3] ✉, E. Leistenschneider[1,2,6], R. Jain[1,2,3], G. Bollen[1,2,3], S. A. Giuliani[1,4,5], K. Lund[1,2], W. Nazarewicz[1,3], L. Neufcourt[1], C. R. Nicoloff[1,2,3], D. Puentes[1,2,3], R. Ringle[1,2], C. S. Sumithrarachchi[1,2] and I. T. Yandow[1,2,3]

Protons and neutrons in the atomic nucleus move in shells analogous to the electronic shell structures of atoms. The nuclear shell structure varies as a result of changes in the nuclear mean field with the number of neutrons *N* and protons *Z*, and these variations can be probed by measuring the mass differences between nuclei. The $N=Z=40$ self-conjugate nucleus ^{80}Zr is of particular interest, as its proton and neutron shell structures are expected to be very similar, and its ground state is highly deformed. Here we provide evidence for the existence of a deformed double-shell closure in ^{80}Zr through high-precision Penning trap mass measurements of $^{80-83}$Zr. Our mass values show that ^{80}Zr is substantially lighter, and thus more strongly bound than predicted. This can be attributed to the deformed shell closure at $N=Z=40$ and the large Wigner energy. A statistical Bayesian-model mixing analysis employing several global nuclear mass models demonstrates difficulties with reproducing the observed mass anomaly using current theory.

Understanding the mechanisms of structural evolution, especially for nuclei far from the beta stability line, is a major challenge in nuclear science[1,2]. In this context, a rich territory for studies of basic nuclear concepts is the neutron-deficient region around mass number $A=80$ (ref. [3]). The properties of the nuclei in this region change rapidly with varying proton and neutron numbers. Indeed, some of these nuclei are among the most deformed in the nuclear chart and exhibit collective behaviour, while others show non-collective excitation patterns characteristic of spherical systems.

The appearance of strongly deformed configurations around ^{80}Zr has been attributed to the population of the intruder $g_{9/2}$ orbitals separated by the spherical $N=Z=40$ subshell closure from the upper *pf* shell. This particular shell structure results in coexisting configurations of different shapes predicted by theory[4–9]. In particular, for the nucleus ^{80}Zr, spherical and deformed (prolate, oblate and triaxial) structures are expected to coexist at low energies, and their competition strongly depends on the size of the calculated spherical $N=Z=40$ gap[10]. Experimentally, ^{80}Zr has a very large quadrupole deformation parameter $\beta_2\approx0.4$ (refs. [11,12]) indicating that the nucleus is prolate in shape. Within the mean-field theory, this has been attributed to the appearance of a large deformed gap at $N=Z=40$ in the deformed single-particle spectrum[5]. Consequently, the nucleus ^{80}Zr can be viewed as a deformed doubly magic system.

In addition to shape-coexistence effects, ^{80}Zr is a great laboratory for isospin physics. Having equal numbers of protons and neutrons, this nucleus is self-conjugate, so it offers a unique venue to study proton–neutron pairing, isospin breaking effects and the Wigner energy reflecting an additional binding in self-conjugate nuclei and their neighbours[13,14].

The mass of an isotope is a sensitive indicator of the underlying shell structure as it reflects the net energy content of a nucleus, including the binding energy. Hence, doubly magic nuclei are substantially lighter, or more bound, than their neighbours. Owing to a lack of precision mass measurement data on ^{80}Zr and its neighbours, it is difficult to characterize the size of the shell effect responsible for the large deformation of ^{80}Zr. To this end, we performed high-precision Penning trap mass spectrometry of four neutron-deficient zirconium isotopes ($^{80-83}$Zr) and analysed the local trends of the binding-energy surface by studying several binding-energy indicators. To quantify our findings, the experimental patterns were interpreted using global nuclear mass models augmented by a Bayesian model averaging (BMA) analysis[15], as described in Methods.

Experimental procedure

The $^{80-83}$Zr isotopes are highly neutron-deficient unstable radioisotopes of zirconium with half-lives ranging between 4.6 s and 42 s (ref. [16]), so they must be produced in specialized facilities and probed using fast and sensitive instrumentation. A schematic of the experimental set-up and procedure is shown in Fig. 1. The Zr isotopes were produced at the National Superconducting Cyclotron Laboratory's Coupled Cyclotron Facility via projectile fragmentation of a 140 MeV u^{-1} ^{92}Mo primary beam impinged on a thin Be target. The produced Zr nuclei were separated from other fragments by the A1900 fragment separator[17] and sent to the advanced cryogenic gas stopper[18], where they were stopped as ions. The ions were extracted from the gas stopper as a low-energy (30 keV Q^{-1}) continuous beam and selected by their mass-to-charge ratio (A/Q) using a dipole magnet. The ions were then sent to the Low Energy Beam and Ion Trap (LEBIT) facility[19]. ^{80,82}Zr ions were sent as singly charged oxides ($A/Q=96$ and 98, respectively) and ^{81,83}Zr ions were sent bare and doubly charged ($A/Q=40.5$ and 41.5, respectively).

[1]Facility for Rare Isotope Beams, Michigan State University, East Lansing, MI, USA. [2]National Superconducting Cyclotron Laboratory, Michigan State University, East Lansing, MI, USA. [3]Department of Physics and Astronomy, Michigan State University, East Lansing, MI, USA. [4]European Centre for Theoretical Studies in Nuclear Physics and Related Areas (ECT-FBK), Trento, Italy. [5]Department of Physics, Faculty of Engineering and Physical Sciences, University of Surrey, Guildford, UK. [6]Present address: CERN, Geneva, Switzerland. ✉e-mail: hamaker@nscl.msu.edu

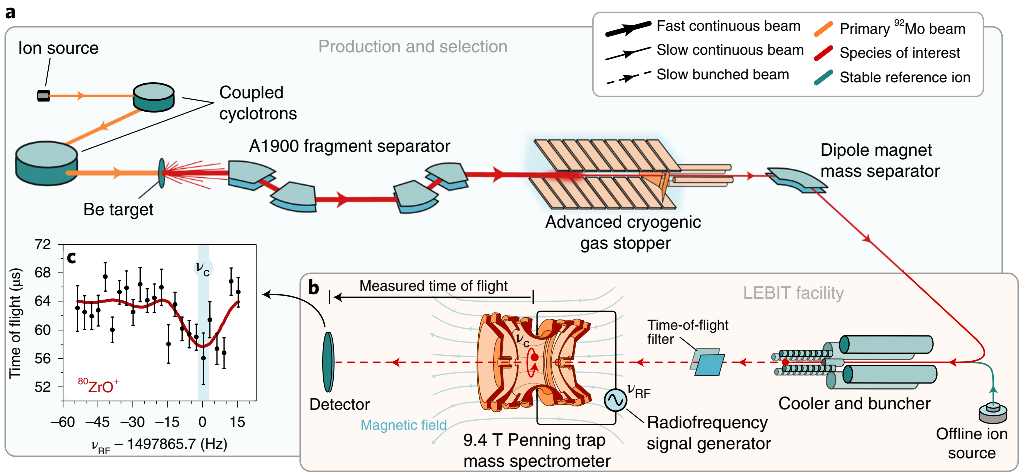

Fig. 1 | The experimental procedure. a, The radioactive Zr isotopes are produced from the fragmentation of an accelerated ^{92}Mo beam as it collides with a Be target. The fast fragments of interest are separated, stopped and delivered at low energies to the LEBIT facility, where the experiment is performed. **b**, At LEBIT, the ion beam is accumulated into low-emittance bunches, which are sent to the Penning trap mass spectrometer for a mass measurement. In the trap, the ion is subjected to a radiofrequency field and then expelled towards a timing detector. When the frequency of the applied field matches the ion's cyclotron frequency (ν_c), the motion of the ion in the trap is resonantly excited, which translates into a shorter time of flight to the detector. **c**, Sample time-of-flight spectrum of an ^{80}Zr^{16}O$^+$ molecular ion obtained by scanning the applied radiofrequency field. The dip in time of flight allows for the determination of the ion's cyclotron frequency, and thus its mass. The red curve is an analytical fit to the data. The error bars represent the statistical uncertainty of the time-of-flight measurement, and the light blue band shows the 1σ uncertainty of the cyclotron frequency determination. See main text and Methods for details.

Table 1 | Results from our mass measurements

Isotope	Ion	Ion ref.	$\bar{R}$	Mass excess	AME20[23]	Difference
^{80}Zr	^{80}Zr^{16}O$^+$	^{85}Rb$^+$	1.129,829,01 (99)	−55,128 (80)	−54,760 (300)[a]	−370 (310)
^{81}Zr	^{81}Zr^{2+}	^{41}K$^+$	0.987,971,08 (13)	−57,556 (10)	−57,524 (92)	−32 (93)
^{82}Zr	^{82}Zr^{16}O$^+$	^{87}Rb$^+$	1.126,770,338 (31)	−63,618.6 (2.5)	−63,614.1 (1.6)	−4.5 (3.0)
^{83}Zr	^{83}Zr^{2+}	^{41}K$^+$	1.012,274,829,7 (85)	−65,916.33 (65)	−65,911.7 (6.4)	−4.7 (6.5)

The mass excesses are relative to the mass number of the isotopes of interest. The weighted average frequency ratio, $\bar{R}$, between the ion of interest (Ion) and the reference ion (Ion ref.) is presented. The results are compared with the mass excesses recommended by the AME20[23]. All mass excesses are in kiloelectronvolts (keV). 1σ uncertainties are shown in parentheses. [a]Extrapolated value based on trends of the mass surface.

On entering the LEBIT facility, the ions first passed through the cooler and buncher[20], where they were accumulated, cooled and released as short bunches to the LEBIT 9.4 T Penning trap[21]. A series of purification techniques (described in Methods) were used to ensure that nearly pure samples of the ion of interest were used for the measurement. A schematic of the LEBIT set-up is shown in Fig. 1b.

In the Penning trap, the mass m_{ion} of an ion with charge q was determined by measuring the cyclotron frequency $\nu_c = qB/(2\pi m_{\mathrm{ion}})$ of the ion's motion about the trap's magnetic field, which has a strength B. The cyclotron frequency ν_c was measured using the time-of-flight ion cyclotron resonance (TOF-ICR) technique[22], as shown in Fig. 1 and described in Methods. The theoretical line shapes[22] for the TOF-ICR spectra were fit to the data, allowing determination of the cyclotron frequency. A sample ^{80}Zr^{16}O$^+$ TOF-ICR spectrum and its theoretical line shape are shown in Fig. 1c.

Before and after each measurement of the ion of interest, measurements of a reference ion were performed to calibrate the magnetic field. The reference ions (^{41}K$^+$, ^{85,87}Rb$^+$) were provided by an offline ion source. The masses of the ions of interest were obtained from the ratio (R) of the cyclotron frequencies of the reference ion ($\nu_{c,\mathrm{ref}}$) and the ion of interest:

$$R = \frac{\nu_{c,\mathrm{ref}}}{\nu_c} = \frac{m_{\mathrm{ion}}/q_{\mathrm{ion}}}{(m_{\mathrm{ref}} - q_{\mathrm{ref}}\, m_e)/q_{\mathrm{ref}}}, \qquad (1)$$

where q_{ion} is the charge state of the ion of interest, m_e is the mass of the electron and m_{ref} and q_{ref} are the atomic mass and charge state of the reference species. The atomic mass m of the Zr isotope of interest is calculated from the mass of the measured ion, accounting for removed electrons and molecular counterparts, where applicable. The results of the measurements are presented in Table 1 and compared with the atomic mass evaluation of 2020 (AME20)[23]. Further details on the measurement, calibration and uncertainty determination procedures are provided in Methods.

Our mass measurement results are in good agreement with the mass values recommended by AME20[23], and provide an improvement of one order of magnitude or more to the precision of the ^{80,81,83}Zr masses. The AME20 values for $^{81-83}$Zr are derived mainly from previous high-precision mass measurements. Penning trap mass measurements of ^{82,83}Zr form the basis of the AME20 mass values for these isotopes[24,25], while a recent storage ring measurement[26] dominates the AME20 mass of ^{81}Zr. Our measurement of ^{82}Zr has the largest discrepancy from AME20, with a value 1.5σ lower. The mass of ^{80}Zr listed in AME20 is an extrapolated value calculated from neighbouring known nuclei using smooth trends of the mass surface. It is worth noting that two previous mass measurements of ^{80}Zr have not been included in the AME. A measurement with only a single event[27] yielded a mass excess of −55.5 (1.5) MeV. The second measurement[28], albeit more precise with a mass excess of −55,647 (150) keV, has not been included in the AME, because

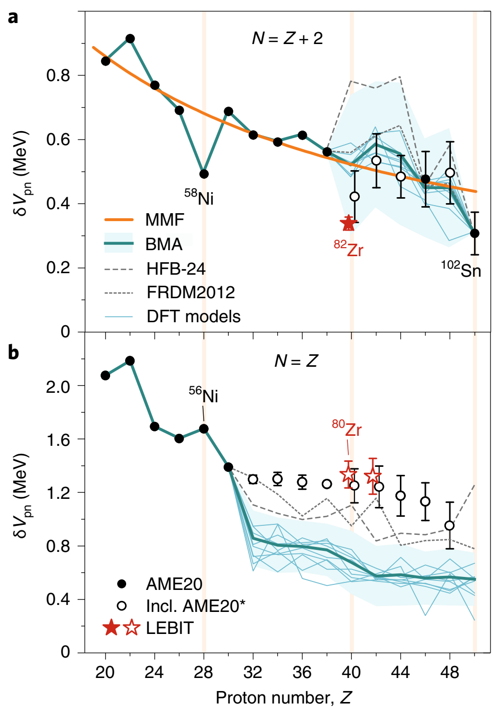

Fig. 2 | Comparison of experimental results with theoretical predictions. **a**,**b**, The effect of the anomalous mass of ^{80}Zr on the mass indicator δV_{pn}: a substantial decrease from the baseline in the $N=Z+2$ sequence (**a**) and a slight increase in the $N=Z$ sequence (**b**), which mirrors the behaviour of other doubly magic nuclei (for example, ^{56}Ni and ^{100}Sn). Black circles represent mass data from the AME20[23]. Red stars include data from this work. Filled symbols (both circles and stars) include only experimental mass values from AME20[23]. Open symbols include mass extrapolations (AME20*) from AME20[23]. All symbols include 1σ error bars. In many cases the error bars are too small to see. The MMF prediction is shown as an orange line in **a**. The thick teal line is the BMA result based on several nuclear models (thin solid lines, DFT models; thin dashed lines, HFB-24 and FRDM2012 models, which include the Wigner energy correction) and the light teal band represents the uncertainty of the BMA approach. See Methods for details about the BMA. The vertical bands denote the magic numbers 28 and 50 as well as the proton number of Zr, $Z=40$.

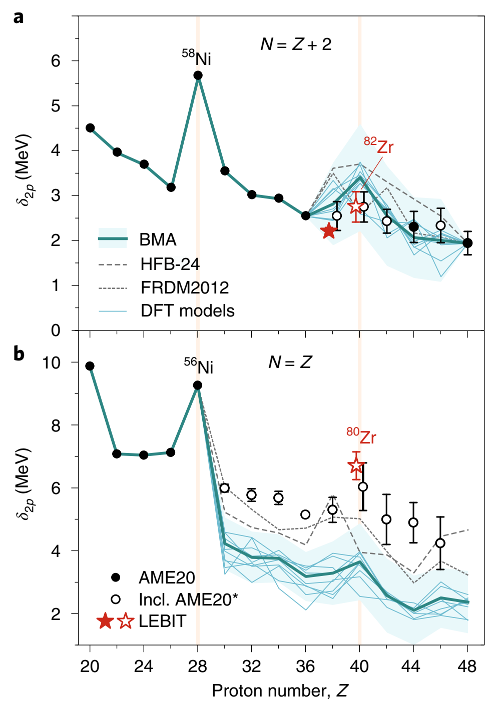

Fig. 3 | Two-proton shell gap. **a**,**b**, The effect of the anomalous mass of ^{80}Zr on the mass indicator δ_{2p}: a decrease from the baseline in the $N=Z+2$ sequence (**a**) and a corresponding increase in the $N=Z$ sequence (**b**). Black circles represent mass data from AME20[23]. Red stars include data from this work. Filled symbols (both circles and stars) include only experimental mass values from AME20[23]. Open symbols include mass extrapolations (AME20*) from AME20[23]. All symbols include 1σ error bars. In many cases the error bars are too small to see. The thick teal line is the BMA result based on several nuclear models (thin solid lines, DFT models; thin dashed lines, HFB-24 and FRDM2012 models, which include the Wigner-energy correction) and the light teal band represents the uncertainty of the BMA approach. See Methods for details on the BMA. The vertical bands denote the magic number 28 and the proton number of Zr, $Z=40$.

other isotopes measured in the same experiment were in disagreement with more recent high-precision results.

The anomalous mass of ^{80}Zr

Our mass measurement of ^{80}Zr reveals that this nucleus is substantially more bound than expected from systematic trends. Indeed, high-quality extrapolations of the mass surface towards ^{80}Zr have been produced by the AME collaboration and others; this has been especially motivated by the astrophysical importance of this nucleus for X-ray bursts[29]. Our mass value is 370 (310) keV/c^2 more bound than the extrapolated value from AME20[23], and 950 (260) keV/c^2 more bound than the Lanzhou extrapolated value[26].

To study the impact of our measurement, we employed various binding-energy differences (described in Methods), adopting our mass values for $^{80-83}$Zr. All other masses used in the calculations were taken from AME20 unless stated otherwise. Along the $N=Z$ line, nuclei are known to be exceptionally well bound as neutrons and protons occupy the same shell model orbitals. Therefore, a useful indicator is the double mass difference δV_{pn} (refs. [30,31]), as defined in Methods.

In Fig. 2a,b, we show δV_{pn} for the $N=Z+2$ and $N=Z$ sequences, respectively. For nuclei away from $N=Z$, the overall behaviour of δV_{pn} is well described by the macroscopic mass formula[31,32] (MMF), $\delta V_{pn}\approx 2(a_{sym}+a_{ssym}A^{-1/3})/A$, where a_{sym} and a_{ssym} are, respectively, the symmetry and surface-symmetry energy coefficients. In the MMF plotted in Fig. 2a, we used $a_{sym}=35$ MeV and $a_{ssym}=-59$ MeV, which were determined by a fit to the data, neglecting the outliers at $A=58$, 82 and 102. Along the $N=Z$ sequence, δV_{pn} is strongly impacted by the Wigner energy[13], the behaviour of which is more convoluted. Moreover, mass data beyond $N=Z$ are scarce in the investigated region. Consequently, if some masses required for the δV_{pn} determination were not experimentally available, we used the recommended values from AME20[23] instead.

Although δV_{pn} is expected to vary smoothly overall, fluctuations around the average trend carry important structural information[30,31,33]. Binding-energy outliers, especially those found in magic nuclei along the $N=Z$ line, result in δV_{pn} deviations for both $N=Z$ and $N=Z+2$ sequences. Considering the $N=Z+2$ results with our masses, the value of δV_{pn} for ^{82}Zr (which is reliant on the mass of ^{80}Zr) is a clear outlier, being 185 keV lower than the MMF trend. This anomaly is similar to those found in ^{58}Ni and ^{102}Sn that are associated with the increased binding energies of the doubly magic self-conjugate nuclei ^{56}Ni and ^{100}Sn. The increased binding energy of ^{80}Zr also impacts the $N=Z$ trends, resulting in increasing values of δV_{pn} for Zr and Mo.

Analogous outliers can also be found by inspecting other mass filters at ^{80}Zr, such as the two-proton shell gap δ_{2p}, commonly

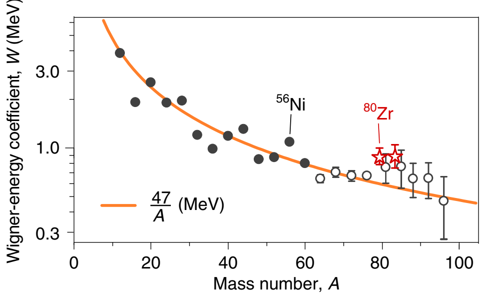

Fig. 4 | Wigner energy. The Wigner-energy coefficient $W(A)$ extracted from δV_{pn} values according to ref. [13]. Black circles represent mass data from AME20[23]. Red stars include data from this work. Open symbols include AME20 mass extrapolations (AME20*). The average trend of ref. [13] is shown by a thick orange line. All symbols include 1σ error bars. In many cases the error bars are too small to see.

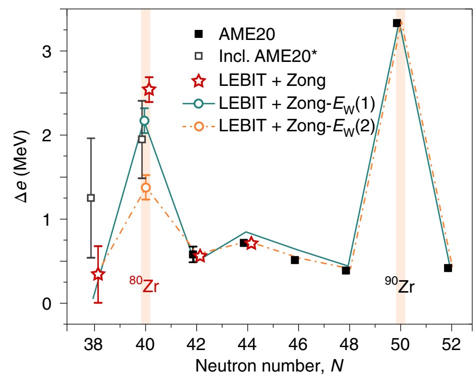

Fig. 5 | Single-particle energy splitting. The empirical single-particle energy gap $\Delta e(N)$ at the Fermi level for the chain of even–even Zr isotopes extracted from nuclear binding energies according to ref. [36]. Black squares represent mass data from AME20[23]. Open grey squares include AME20 mass extrapolations (AME20*). Open stars represent the data from this work augmented by mass extrapolations from ref. [38]. These values of Δe were further corrected by removing contributions from the Wigner-energy term $E_W(1)$ (solid line; ref. [39]) or $E_W(2)$ (dash-dotted line; ref. [13]). See Methods for the definition of E_W. No uncertainty is assigned to $E_W(1)$ or $E_W(2)$, so the error bars for the corrected Δe values match those of the corresponding uncorrected values. The corrected Δe error bars are only shown for ^{80}Zr. All error bars represent 1σ uncertainty. In many cases the error bars are too small to see. The vertical bands denote shell closures at $N=40$ and $N=50$.

employed in tests of shell closures[34,35]. The δ_{2p} mass filter as a function of proton number for both the $N=Z$ and $N=Z+2$ sequences is shown in Fig. 3 (additional discussion is provided in Methods).

The results shown in Fig. 2 provide compelling empirical evidence for the existence of a deformed shell closure in ^{80}Zr. One needs to bear in mind, however, that ^{80}Zr is a self-conjugate system and some additional contribution to its binding energy comes from the Wigner energy. Usually, the Wigner term in even–even nuclei is parameterized as $E_W=a_W|N-Z|/A$. As discussed in ref. [13] and Methods, the Wigner-energy coefficient $W(A)=a_W/A$ can be empirically extracted from the values of δV_{pn}. Our data, shown in Fig. 4, indicate that the value of $W(A)$ at ^{80}Zr and ^{56}Ni is locally enhanced, in contrast to the gradually decreasing trend for heavier $N=Z$ nuclei that is well captured by the value of $a_W=47$ MeV obtained in ref. [13]. A note of caution is in order: some contribution to the local increase of the empirical value of W in ^{80}Zr and ^{56}Ni can be attributed to the enhanced binding due to their shell structures. The contributions of the Wigner energy and shell structure will be disentangled with another mass filter in the following paragraph.

Experimental masses offer a way to assess the size of the deformed $N=40$ single-particle gap. This can be done by employing the filter $\Delta e(N=2n)$[36], which provides an estimate of the single-particle energy gap $e_{n+1}-e_n$ at the Fermi level. Figure 5 shows Δe for the Zr isotopic chain (see ref. [37] for applications of Δe to the K and Ca chains). Some masses of proton-rich Zr isotopes needed to determine Δe are not known experimentally, so these have been taken from mass relations of mirror nuclei by Zong and others[38]. It is seen that Δe reaches a maximum for ^{90}Zr at the spherical magic number $N=50$ and a local maximum for ^{80}Zr at the deformed magic number $N=40$. Because the latter value can be affected by the Wigner energy, we removed the binding-energy contribution from E_W by applying two models: $E_W(1)$[39] and $E_W(2)$[13]. The resulting correction to Δe practically affects only the $N=40$ value. As discussed in Methods, the expression $E_W(1)$ is well localized at $N=Z$ and reduces Δe by ~300 keV. The expression $E_W(2)$ decreases linearly with the neutron excess, and the corresponding reduction of Δe is ~1.1 MeV. Even in this case, the energy gap at $N=40$ is a factor of 2–3 larger than Δe for $42\leq N\leq 48$. Although the size of this gap is reduced compared to the spherical $N=50$ gap, it is characteristic of a deformed shell closure. The strong shell effect comes from the self-conjugate nature of ^{80}Zr as the deformed proton and neutron shell effects reinforce one another.

Bayesian analysis of mass models

To obtain improved theoretical mass predictions in the ^{80}Zr region, we conducted a Bayesian statistical analysis combining Gaussian process extrapolation and BMA[40] of 11 theoretical global mass models following the same procedure as in refs. [15,41]. The BMA framework uses the collective wisdom of the models, constrained by data, to make predictions and quantify uncertainties. Details of the individual models and the BMA methodology are provided in Methods.

The BMA predictions for δV_{pn} are shown in Fig. 2a,b. The predictions for $N=Z+2$ are well constrained outside the region $38<Z<50$ due to the wealth of experimental mass data. In the region $38\leq Z\leq 50$, the BMA results are consistent with the AME20 data and the MMF trend. At $Z=40$, the experimental δV_{pn} value, which includes our ^{80,82}Zr mass results, falls just within the error band. The BMA result for δV_{pn} along the $N=Z$ line in the region $Z>30$ does not agree with either the AME20 extrapolations or the experimental value at $Z=40$. Two of the models, FRDM2012[42] and HFB-24[39], which include the phenomenological Wigner term, perform slightly better than the density functional theory (DFT) models. However, they still fall short of the experimental trends, probably due to underestimation of the Wigner energy. Indeed, the value of a_W in FRDM2012[42] is 30 MeV, which is much less than the $a_W=47$ MeV representing the average trend seen in Fig. 4. The Wigner energy $E_W(1)$ of HFB-24 is even smaller. The BMA predictions for δ_{2p} are shown in Fig. 3a,b and trends similar to those seen in the δV_{pn} results are observed.

In summary, the interplay between theory and experiment was crucial in understanding this region of the nuclear chart. Although the deformed shell gap at $N=Z=40$ was predicted over 30 years ago[4,5], a lack of precise experimental data has prevented a quantitative assessment of the gap's size until now. To further refine the deformed shell closure, high-precision mass measurements in this region are needed, which will be made possible with next-generation radioactive ion beam facilities and mass measurement techniques.

Online content

Any methods, additional references, Nature Research reporting summaries, source data, extended data, supplementary information, acknowledgements, peer review information; details of author contributions and competing interests; and statements of data and code availability are available at https://doi.org/10.1038/s41567-021-01395-w.

Received: 21 May 2021; Accepted: 17 September 2021;
Published online: 25 November 2021

References

1. National Research Council *Nuclear Physics*: *Exploring the Heart of Matter* (The National Academies Press, 2013).
2. Otsuka, T., Gade, A., Sorlin, O., Suzuki, T. & Utsuno, Y. Evolution of shell structure in exotic nuclei. *Rev. Mod. Phys.* **92**, 015002 (2020).
3. Eberth, J., Meyer, R. A. & Sistemich, K. *Nuclear Structure of the Zirconium Region* (Springer, 1988).
4. Hamilton, J. H. et al. Effects of reinforcing shell gaps in the competition between spherical and highly deformed shapes. *J. Phys. G* **10**, L87–L91 (1984).
5. Nazarewicz, W., Dudek, J., Bengtsson, R., Bengtsson, T. & Ragnarsson, I. Microscopic study of the high-spin behaviour in selected $A\simeq80$ nuclei. *Nucl. Phys. A* **435**, 397–447 (1985).
6. Petrovici, A., Schmid, K. & Faessler, A. Shape coexistence and shape transition in $N\approx Z$ nuclei from krypton to molybdenum. *Nucl. Phys. A* **605**, 290–300 (1996).
7. Gaudefroy, L. et al. Collective structure of the $N=40$ isotones. *Phys. Rev. C* **80**, 064313 (2009).
8. Rodríguez, T. R. & Egido, J. L. Multiple shape coexistence in the nucleus ^{80}Zr. *Phys. Lett. B* **705**, 255–259 (2011).
9. Kaneko, K., Shimizu, N., Mizusaki, T. & Sun, Y. Triple enhancement of quasi-SU(3) quadrupole collectivity in strontium-zirconium $N\approx Z$ isotopes. *Phys. Lett. B* **817**, 136286 (2021).
10. Reinhard, P.-G. et al. Shape coexistence and the effective nucleon-nucleon interaction. *Phys. Rev. C* **60**, 014316 (1999).
11. Lister, C. J. et al. Gamma radiation from the $N=Z$ nucleus $^{80}_{40}\mathrm{Zr}_{40}$. *Phys. Rev. Lett.* **59**, 1270–1273 (1987).
12. Llewellyn, R. D. O. et al. Establishing the maximum collectivity in highly deformed $N=Z$ nuclei. *Phys. Rev. Lett.* **124**, 152501 (2020).
13. Satuła, W., Dean, D., Gary, J., Mizutori, S. & Nazarewicz, W. On the origin of the Wigner energy. *Phys. Lett. B* **407**, 103–109 (1997).
14. Bentley, I. & Frauendorf, S. Relation between Wigner energy and proton-neutron pairing. *Phys. Rev. C* **88**, 014322 (2013).
15. Neufcourt, L. et al. Quantified limits of the nuclear landscape. *Phys. Rev. C* **101**, 044307 (2020).
16. *Evaluated Nuclear Structure Data File* (ENSDF, accessed 25 March 2021); https://www.nndc.bnl.gov/ensarchivals
17. Morrissey, D., Sherrill, B., Steiner, M., Stolz, A. & Wiedenhoever, I. Commissioning the A1900 projectile fragment separator. *Nucl. Instrum. Methods Phys. Res. B* **204**, 90–96 (2003).
18. Lund, K. et al. Online tests of the advanced cryogenic gas stopper at NSCL. *Nucl. Instrum. Methods Phys. Res. B* **463**, 378–381 (2020).
19. Ringle, R., Schwarz, S. & Bollen, G. Penning trap mass spectrometry of rare isotopes produced via projectile fragmentation at the LEBIT facility. *Int. J. Mass Spectrom.* **349–350**, 87–93 (2013).
20. Schwarz, S., Bollen, G., Ringle, R., Savory, J. & Schury, P. The LEBIT ion cooler and buncher. *Nucl. Instrum. Methods Phys. Res. A* **816**, 131–141 (2016).
21. Ringle, R. et al. The LEBIT 9.4 T Penning trap mass spectrometer. *Nucl. Instrum. Methods Phys. Res. A* **604**, 536–547 (2009).
22. König, M., Bollen, G., Kluge, H.-J., Otto, T. & Szerypo, J. Quadrupole excitation of stored ion motion at the true cyclotron frequency. *Int. J. Mass Spectrom. Ion Process.* **142**, 95–116 (1995).
23. Huang, W., Wang, M., Kondev, F., Audi, G. & Naimi, S. The AME 2020 atomic mass evaluation (I). Evaluation of input data, and adjustment procedures. *Chin. Phys. C* **45**, 030002 (2021).
24. Kankainen, A. et al. Mass measurements of neutron-deficient nuclides close to $A=80$ with a Penning trap. *Eur. Phys. J. A* **29**, 271–280 (2006).
25. Vilén, M. et al. High-precision mass measurements and production of neutron-deficient isotopes using heavy-ion beams at IGISOL. *Phys. Rev. C* **100**, 054333 (2019).
26. Xing, Y. et al. Mass measurements of neutron-deficient Y, Zr and Nb isotopes and their impact on *rp* and νp nucleosynthesis processes. *Phys. Lett. B* **781**, 358–363 (2018).
27. Issmer, S. et al. Direct mass measurements of $A=80$ isobars. *Eur. Phys. J. A* **2**, 173–177 (1998).
28. Lalleman, A. S. et al. Mass measurements of exotic nuclei around $N=Z=40$ with CSS2. *Hyperfine Interact.* **132**, 313–320 (2001).
29. Schatz, H. & Ong, W.-J. Dependence of X-ray burst models on nuclear masses. *Astrophys. J.* **844**, 139 (2017).
30. Zhang, J.-Y., Casten, R. & Brenner, D. Empirical proton-neutron interaction energies. Linearity and saturation phenomena. *Phys. Lett. B* **227**, 1–5 (1989).
31. Stoitsov, M., Cakirli, R. B., Casten, R. F., Nazarewicz, W. & Satuła, W. Empirical proton-neutron interactions and nuclear density functional theory: global, regional and local comparisons. *Phys. Rev. Lett.* **98**, 132502 (2007).
32. Reinhard, P.-G., Bender, M., Nazarewicz, W. & Vertse, T. From finite nuclei to the nuclear liquid drop: leptodermous expansion based on self-consistent mean-field theory. *Phys. Rev. C* **73**, 014309 (2006).
33. Bender, M. & Heenen, P.-H. What can be learned from binding energy differences about nuclear structure: the example of δV_{pn}. *Phys. Rev. C* **83**, 064319 (2011).
34. Bender, M. et al. The $Z=82$ shell closure in neutron-deficient Pb isotopes. *Eur. Phys. J. A* **14**, 23–28 (2002).
35. Lunney, D., Pearson, J. M. & Thibault, C. Recent trends in the determination of nuclear masses. *Rev. Mod. Phys.* **75**, 1021–1082 (2003).
36. Satuła, W., Dobaczewski, J. & Nazarewicz, W. Odd-even staggering of nuclear masses: pairing or shape effect? *Phys. Rev. Lett.* **81**, 3599–3602 (1998).
37. Koszorús, Á. et al. Charge radii of exotic potassium isotopes challenge nuclear theory and the magic character of $N=32$. *Nat. Phys.* **17**, 439–443 (2021).
38. Zong, Y. Y., Ma, C., Zhao, Y. M. & Arima, A. Mass relations of mirror nuclei. *Phys. Rev. C* **102**, 024302 (2020).
39. Goriely, S., Chamel, N. & Pearson, J. M. Further explorations of Skyrme-Hartree-Fock-Bogoliubov mass formulas. XIII. The 2012 atomic mass evaluation and the symmetry coefficient. *Phys. Rev. C* **88**, 024308 (2013).
40. Phillips, D. R. et al. Get on the BAND wagon: a Bayesian framework for quantifying model uncertainties in nuclear dynamics. *J. Phys. G* **48**, 072001 (2021).
41. Neufcourt, L. et al. Beyond the proton drip line: Bayesian analysis of proton-emitting nuclei. *Phys. Rev. C* **101**, 014319 (2020).
42. Möller, P., Sierk, A., Ichikawa, T. & Sagawa, H. Nuclear ground-state masses and deformations: FRDM(2012). *Atom. Data Nucl. Data Tables* **109–110**, 1–204 (2016).

Methods

The TOF-ICR technique for cyclotron frequency determination. In a Penning trap, an ion is confined in space by the superposition of a weak axially harmonic electric potential and a strong homogeneous magnetic field, oriented in the axial direction. In the absence of the electric field, the ion performs a circular motion about the axis of the magnetic field at cyclotron frequency ν_c, the measurement of which allows the determination of the mass of the particle. The introduction of the electric field disturbs the cyclotron motion, which is split into two independent radial components: the reduced cyclotron and the much slower magnetron precession (with frequencies ν_+ and ν_-, respectively). The 'free' cyclotron frequency is determined by measurement of the $\nu_c = \nu_+ + \nu_-$ sideband. This quantity is nearly invariant with respect to fluctuations in the trapping electric field, which grants Penning trap mass spectrometry great accuracy[43].

In the TOF-ICR technique, the sideband is determined by applying an external quadrupole radiofrequency field (with frequency ν_{RF}) to the ion, which converts one eigenmotion into another. The ion is initially prepared in a pure magnetron motion, which, at LEBIT, is done through the Lorentz steering technique[44]. On application of the external field, if the resonant condition $\nu_{RF} = \nu_+ + \nu_-$ is met, the conversion from pure magnetron motion to pure reduced cyclotron motion occurs. The conversion is probed by measuring the ion's time of flight from the trap to a microchannel plate detector outside the magnetic field. If the ion in the trap is in a pure reduced cyclotron motion, which holds greater kinetic energy, the time of flight is reduced. Figure 1b provides a schematic of the TOF-ICR set-up.

In a typical TOF-ICR procedure, ν_{RF} is scanned to characterize the resonant reduction of the time of flight, generating spectra such as the one shown in Fig. 1c. The width of the resonance, which determines the precision of the ν_c measurement, is inversely proportional to the time for which the external excitation field is applied. In the measurements described herein, both continuous[22] and Ramsey[45] radiofrequency quadrupolar excitation schemes were used, with excitation times ranging from 50 ms to 1 s. The cyclotron frequency is determined through an analytical fit to the time-of-flight spectrum, the line shapes of which are described in the literature for both used excitation schemes[22,45].

Mass determination from cyclotron frequencies. Here we describe in greater detail the procedure used to extract atomic mass values for the isotopes of interest from the measured cyclotron frequencies. As explained in the main text, each measurement of the cyclotron frequency ν_c of the ion of interest is interleaved by measurements of the cyclotron frequency of the reference ion, $\nu_{c,ref}$. Reference ions were chosen as singly ionized species of widely available stable alkali atoms whose masses (m_{ref}) are well known in the literature[23], as well as whose A/Q is close to the ion of interest to avoid large mass-dependent systematic shifts in the calibration procedure. The frequency ratio (1) for each measurement of ν_c was calculated using the time-interpolated cyclotron frequency from the reference measurements to the time of the measurement of the ion of interest. In total, three measurements of R were performed for the $^{83}Zr^{2+}$–$^{41}K^+$ pair, six for the $^{82}ZrO^+$–$^{87}Rb^+$ pair, five for the $^{81}Zr^{2+}$–$^{41}K^+$ pair and four for the $^{80}ZrO^+$–$^{85}Rb^+$ pair. The masses of each ion of interest (m_{ion}) presented in Table 1 were calculated with equation (1), using the average of multiple frequency ratios ($\bar{R}$) weighted by their uncertainties.

The atomic masses (m) of the Zr isotopes of interest were calculated using $m = m_{ion} + qm_e - m_{mol}$, where m_{mol} is the atomic mass of the molecular counterpart (^{16}O in the case of $^{80,82}Zr$ only). The electron binding energies and molecular binding energies of $^{80,82}ZrO^+$ were disregarded as they are on the order of electronvolts, which is several orders of magnitude lower than the statistical uncertainty of the measurement. Mass excesses, defined as the difference between the atomic mass and the isotope's mass number, are reported in Table 1 for the measured Zr isotopes.

Evaluation of uncertainties. Uncertainties related to the extraction of cyclotron frequencies from the fits dominate the statistical error budget. Systematic errors arise from magnetic field inhomogeneities, trapping potential imperfections and a possible misalignment between the trap and magnetic field[46]. These errors result in a shift in the average frequency ratio, which scales linearly with the difference in mass between the ion of interest and the reference ion. The mass-dependent shifts in $\bar{R}$ have been measured at the LEBIT facility and found to be $\Delta\bar{R} = 2 \times 10^{-10}\ \mathrm{u}^{-1}$ (ref. [47]). This shift has been folded into the ratios and uncertainties reported in Table 1.

Other systematic errors on the individual measured frequency ratios R must be taken into account separately. Nonlinear magnetic field fluctuations in time can result in calibration errors. This effect has been studied at LEBIT and leads to a shift in R at a level below 1×10^{-9} per hour[48]. Measurement times ranged from 3 h for ^{80}Zr to 15 min for ^{83}Zr. This uncertainty was folded into the ratio uncertainties, although it had a negligible effect on the final error estimate. Special relativity can have an effect on the cyclotron frequency ratios[49], but this error was negligible compared to the statistical uncertainty. Ion–ion interactions were minimized using several methods. Before entering the trap, the ion bunches from the cooler and buncher were purified using a time-of-flight filter to only allow ions with a specific mass-to-charge ratio to enter the trap. Once captured in the trap, ions were further purified against isobaric contamination using targeted dipole cleaning[50] and the stored waveform inverse Fourier transform (SWIFT) technique[51]. Additional ion–ion interactions were taken into account by performing a count-rate class analysis on each dataset whenever possible[52]. The count-rate class analysis only led to a shift in the ^{83}Zr ratio ($\Delta R = 9.8(7)\times10^{-9}$). This shift has been included in the value reported in Table 1. Finally, Birge ratios were calculated to determine whether inner or outer uncertainties were reported for the final mass uncertainties[53].

Binding-energy indicators. To extract quantities of interest for the experimental mass surface, we used various binding-energy differences (mass filters)[54,55]. These include the following.

The double mass difference δV_{pn} (refs.[30,31,33]) is given by

$$\begin{aligned}\delta V_{\rm pn}(N,Z) &= \tfrac{1}{4}\,[B(N,Z) - B(N-2,Z) \\ &\quad - B(N,Z-2) + B(N-2,Z-2)] \\ &= \tfrac{1}{4}\,[S_{2p}(N,Z) - S_{2p}(N-2,Z)].\end{aligned} \tag{2}$$

The Wigner energy coefficient in an even–even nucleus with $N=Z=A/2$ (ref. [13]) is given by

$$\begin{aligned}W(A) &= \delta V_{\rm pn}(A/2,A/2) \\ &\quad -\tfrac{1}{2}\left[\delta V_{\rm pn}(A/2,A/2-2) + \delta V_{\rm pn}(A/2+2,A/2)\right].\end{aligned} \tag{3}$$

The two-proton shell gap δ_{2p} (refs. [34,35]) is given by

$$\begin{aligned}\delta_{2p}(N,Z) &= 2B(N,Z) - B(N,Z+2) - B(N,Z-2) \\ &= S_{2p}(N,Z) - S_{2p}(N,Z+2).\end{aligned} \tag{4}$$

The three-point mass difference $\Delta_n^{(3)}$ (ref. [36]) is given by

$$\begin{aligned}\Delta_n^{(3)}(N,Z) &= \tfrac{(-1)^N}{2}\,[2B(N,Z) - B(N-1,Z) - B(N+1,Z)] \\ &= \tfrac{(-1)^N}{2}\,[S_n(N,Z) - S_n(N+1,Z)]\end{aligned} \tag{5}$$

The single-particle energy splitting Δe (ref. [36]) is given by

$$\begin{aligned}\Delta e(N,Z) &= e_{n+1} - e_n = 2\left[\Delta_n^{(3)}(N=2n,Z) - \Delta_n^{(3)}(N=2n+1,Z)\right] \\ &= (-1)^N[S_n(N,Z) - S_n(N+2,Z)].\end{aligned} \tag{6}$$

In the above equations, B is the (positive) nuclear binding energy, obtained from the atomic mass of the nucleus. S_{2p} is the two-proton separation energy

$$S_{2p}(N,Z) = B(N,Z) - B(N,Z-2), \tag{7}$$

and S_n is the one-neutron separation energy

$$S_n(N,Z) = B(N,Z) - B(N-1,Z). \tag{8}$$

Wigner-energy parameterizations. The Wigner-energy contribution to the total binding energy produces an additional binding for nuclei close to $N=Z$. In the HFB-24 mass model[39], the Wigner term has been parameterized as

$$E_{\rm W}(1) = V_{\rm W}\mathrm{e}^{-\lambda_{\rm W}\left(\frac{N-Z}{A}\right)^2} + V'_{\rm W}|N-Z|\mathrm{e}^{-\left(\frac{A}{A_0}\right)^2}, \tag{9}$$

where $V_W = 1.8$ MeV, $\lambda_W = 380$, $V'_W = -0.84$ MeV and $A_0 = 26$. In this model, E_W rapidly decreases with $|N-Z|$ when moving away from the $N=Z$ line. In the traditional parameterization of E_W:

$$E_{\rm W}(2) = -a_{\rm W}\frac{|N-Z|}{A}, \tag{10}$$

one assumes that $E_W = 0$ at $N=Z$ and linearly decreases with the neutron excess. In this work, we adopt the value of $a_W = 47$ MeV from ref. [13].

Nuclear models. In this study we considered nine models based on nuclear DFT: SkM*[56], SkP[57], SLy4[58], SV-min[59], UNEDF0[60], UNEDF1[61], UNEDF2[62], D1M[63] and BCPM[64]. Two additional mass models commonly used in nuclear astrophysics studies were also considered: FRDM2012[42] and HFB-24[39].

Three of these models (SkM*, UNEDF0 and FRDM2012) predict large, prolate ground-state deformation for ^{80}Zr around $\beta_2 = 0.39$, in agreement with experiments. HFB-24 predicts an oblate deformed ground state, whereas all the remaining models predict a spherical ground state. Such variations in the predicted ground-state deformation are manifestations of the near-lying coexisting configurations with different shapes expected theoretically, as discussed in the main text. It is important to notice that, although the relative positions of the different minima strongly depend on the underlying interaction[10] and beyond-DFT correlations[8], the energy shifts between the deformed ground-state configuration and the spherical minimum are relatively small[10]. As a consequence, the absolute impact of shape coexistence in the predicted mass value is expected to be minor and can be absorbed by the statistical correction.

Bayesian model averaging. The binding energies $B(N, Z)$ predicted by nuclear mass models were used to compute the two-proton separation energies (equation (7)), which were then used to compute the δV_{pn} mass differences.

For each model employed, we construct the statistical emulator $\delta^{em}_{S_{2p}}$ of separation energy residuals:

$$\delta^{em}_{S_{2p}}(N,Z) := S^{exp}_{2p}(N,Z) - S^{th}_{2p}(N,Z). \tag{11}$$

The predicted separation energies are then given by $S^{em}_{2p}(N,Z) = S^{th}_{2p}(N,Z) + \delta^{em}_{S_{2p}}$. The Bayesian analysis (training and testing) was performed using only experimental data from AME20[23], without the inclusion of AME20 extrapolated values. Seven nuclei (^{48}Ni, ^{54}Zn, ^{84}Zr, ^{86}Mo, ^{90}Ru, ^{92}Ru and ^{94}Pd) placed at the dataset outer boundary were excluded from the training set and were used as independent testing data to compute the BMA evidence weights. For ^{48}Ni and ^{54}Zn we employed the experimental Q_{2p} values from ref. [65] and ref. [66], respectively. Our dataset thus consists of 152 points (x_i, y_i), where $x_i := (N_i, Z_i)$ and $y_i := \delta^{em}_{S_{2p}}(x_i)$. Following the Bayesian methodology described in ref. [15], we constructed emulators for separation energy residuals $\delta^{GP}(N, Z)$ using Gaussian processes (GPs), $\delta^{GP}(x) \sim \mathcal{GP}(\mu, k_{\eta,\rho}(x, x'))$, over the bi-dimensional domain x. The GP is characterized by its mean function and covariance kernel, taken respectively as a constant μ and squared-exponential covariance kernel

$$k_{\eta,\rho}(x,x') := \eta^2 e^{-\frac{(Z-Z')^2}{\rho_Z} - \frac{(N-N')^2}{\rho_N}},$$

where ρ_Z and ρ_N are the correlation ranges along the proton and neutron directions, respectively. The advantage of considering the mean μ as a GP hyperparameter has been discussed in ref. [41].

We add to the model a term accounting for statistical uncertainties, assumed independent, identically distributed and scaled by a parameter σ. Because the experimental uncertainty is small compared to the model uncertainty, following ref. [67], we have chosen to fix the parameter σ to the experimental errors from AME20. This yields

$$y_i = \delta^{GP}(x_i) + \sigma\epsilon_i. \tag{12}$$

Thus our GP model is parameterized by the five-dimensional vector $\theta := (\mu, \eta, \rho_Z, \rho_N, \sigma)$.

Posterior distributions for the $\mathcal{GP}$ parameters are obtained via Bayes' equation:

$$p(y|\theta) := \frac{p(\theta|y)\pi(\theta)}{\int p(\theta|y)\pi(\theta)d\theta}, \tag{13}$$

where $p(\theta|y)$ is the likelihood of the statistical model (equation (12)) and $\pi(\theta)$ the prior on its parameters. Priors were taken as weakly informative, as described in ref. [15]. Samples from the posterior distributions of the $\mathcal{GP}$ parameters were drawn from iterations of a Monte Carlo Markov chain. These samples of the residuals' emulators were in turn used to produce samples of two-proton separation energies and mass filters, as well as derive statistical predictions (averages and corresponding correlated uncertainties along with full covariance matrices).

In a second stage of the analysis, we ensemble the emulators built from each individual nuclear model according to their BMA weights, namely the posterior probability for each model to be the hypothetical true model, assuming it is one of them, given priors on model weights and data. Although the classical BMA literature[68] relies on the same data y as used for the individual model's training, for this step we prefer to use new 'testing' data y^* (^{48}Ni, ^{54}Zn, ^{84}Zr, ^{86}Mo, ^{90}Ru, ^{92}Ru and ^{94}Pd) located at the outer boundary of the training set and excluded from the GP training. This ensures that the weights better reflect the extrapolative power of the models and reduces overfitting. Formally, we can write[15] these BMA weights as

$$w_k = p(\mathcal{M}_k|y^*) = \frac{p(y^*|\mathcal{M}_k)\pi(\mathcal{M}_k)}{\sum_{\ell=1}^{11} p(y|\mathcal{M}_\ell)\pi(\mathcal{M}_\ell)}, \tag{14}$$

where $\pi(\mathcal{M}_k)$ are prior model weights and $p(y|\mathcal{M}_k)$ are the model evidences obtained by integrating the likelihood equation over the parameter space. For our GP emulators, this gives

$$p(y|\mathcal{M}_k) = \int p(y|\theta_k, \mathcal{M}_k)\pi(\theta_k, \mathcal{M}_k)d\theta_k. \tag{15}$$

We assume uniform prior weights, which are, from a statistical standpoint, the unique non-informative prior distribution in this set-up. To speed up computations and increase stability[69], the evidence integrals are calculated using the Laplace approximation[68], where it is assumed that the posterior is Gaussian with the same mean and standard deviation. The resulting model evidences are

$$p(y|\mathcal{M}_k) \approx \exp\left[-\sum_i \frac{\left(y_i^{exp} - y^{(k)}(x_i)\right)^2}{2\sigma_{y_k}(x_i)^2}\right], \tag{16}$$

where $y^{(k)}$ are the individual model emulators' predictions, $\sigma_{y_k}(x)$ the corresponding uncertainties and i runs over the retained set of nuclei[69].

The model weights (rounded to two decimal digits) are $w_k = 0.01$ (SkM*), 0.04 (SkP), 0.12 (SLy4), 0.16 (SV-min), 0.07 (UNEDF0), 0.11 (UNEDF1), 0.20 (UNEDF2), 0.05 (BCPM), 0.21 (D1M), 0.00 (FRDM) and 0.00 (HFB-24). The final BMA predictions are calculated as

$$y(x) = \sum_k w_k y^{(k)}(x) \tag{17}$$

and the associated uncertainties as

$$\sigma_y^2(x) = \sum_k w_k\left(y^{(k)}(x) - y(x)\right)^2 + \sum_k w_k \sigma^2_{y_k}(x). \tag{18}$$

This last equation conveniently splits the uncertainties into the uncertainty on the model choice and the uncertainty on the individual models' parameters, and highlights what would be lost if a single model were used. The estimated S_{2p} values with corresponding uncertainties and covariances are then employed to calculate δV_{pn} and δ_{2p} using equations (2), (4) and (7).

Finally, Fig. 3 displays the two-proton shell gap δ_{2p} (4). For the $N = Z + 2$ sequence, the BMA prediction agrees with experiment within the estimated uncertainty. For $N = Z$, the anomalous mass of ^{80}Zr results in an increase of δ_{2p} above the baseline. Similar to what is seen in Fig. 2b, the HFB-24 and FRDM2012 models that include the Wigner-energy correction lie slightly below the data points. As discussed earlier, this suggests that the Wigner energy term is underestimated by both models.

Data availability
The data that support the plots within this paper and other findings of this study are available from the corresponding author upon reasonable request.

Code availability
Our unpublished computer codes used to generate the results reported in this paper and central to its main claims will be made available upon request.

References

43. Gabrielse, G. Why is sideband mass spectrometry possible with ions in a Penning trap? *Phys. Rev. Lett.* **102**, 172501 (2009).
44. Ringle, R. et al. A 'Lorentz' steerer for ion injection into a Penning trap. *Int. J. Mass Spectrom.* **263**, 38–44 (2007).
45. George, S. et al. The Ramsey method in high-precision mass spectrometry with Penning traps: experimental results. *Int. J. Mass Spectrom.* **264**, 110–121 (2007).
46. Bollen, G., Moore, R. B., Savard, G. & Stolzenberg, H. The accuracy of heavy-ion mass measurements using time of flight-ion cyclotron resonance in a Penning trap. *J. Appl. Phys.* **68**, 4355–4374 (1990).
47. Gulyuz, K. et al. Determination of the direct double-β-decay Q value of ^{96}Zr and atomic masses of $^{90-92,94,96}$Zr and $^{92,94-98,100}$Mo. *Phys. Rev. C* **91**, 055501 (2015).
48. Ringle, R. et al. High-precision Penning trap mass measurements of ^{37,38}Ca and their contributions to conserved vector current and isobaric mass multiplet equation. *Phys. Rev. C* **75**, 055503 (2007).
49. Brown, L. S. & Gabrielse, G. Geonium theory: physics of a single electron or ion in a Penning trap. *Rev. Mod. Phys.* **58**, 233–311 (1986).
50. Blaum, K. et al. Population inversion of nuclear states by a Penning trap mass spectrometer. *Europhys. Lett.* **67**, 586–592 (2004).
51. Kwiatkowski, A. A., Bollen, G., Redshaw, M., Ringle, R. & Schwarz, S. Isobaric beam purification for high precision Penning trap mass spectrometry of radioactive isotope beams with SWIFT. *Int. J. Mass Spectrom.* **379**, 9–15 (2015).
52. Bollen, G. et al. Resolution of nuclear ground and isomeric states by a Penning trap mass spectrometer. *Phys. Rev. C* **46**, R2140–R2143 (1992).
53. Birge, R. T. The calculation of errors by the method of least squares. *Phys. Rev.* **40**, 207–227 (1932).
54. Jänecke, J. & Comay, E. Properties of homogeneous and inhomogeneous mass relations. *Nucl. Phys. A* **436**, 108–124 (1985).
55. Jensen, A., Hansen, P. & Jonson, B. New mass relations and two- and four-nucleon correlations. *Nucl. Phys. A* **431**, 393–418 (1984).
56. Bartel, J., Quentin, P., Brack, M., Guet, C. & Håkansson, H.-B. Towards a better parametrisation of Skyrme-like effective forces: a critical study of the SkM force. *Nucl. Phys. A* **386**, 79–100 (1982).

57. Dobaczewski, J., Flocard, H. & Treiner, J. Hartree-Fock-Bogolyubov description of nuclei near the neutron-drip line. *Nucl. Phys. A* **422**, 103–139 (1984).
58. Chabanat, E., Bonche, P., Haensel, P., Meyer, J. & Schaeffer, R. New Skyrme effective forces for supernovae and neutron rich nuclei. *Phys. Scr.* **T56**, 231–233 (1995).
59. Klüpfel, P., Reinhard, P.-G., Bürvenich, T. J. & Maruhn, J. A. Variations on a theme by Skyrme: a systematic study of adjustments of model parameters. *Phys. Rev. C* **79**, 034310 (2009).
60. Kortelainen, M. et al. Nuclear energy density optimization. *Phys. Rev. C* **82**, 024313 (2010).
61. Kortelainen, M. et al. Nuclear energy density optimization: large deformations. *Phys. Rev. C* **85**, 024304 (2012).
62. Kortelainen, M. et al. Nuclear energy density optimization: shell structure. *Phys. Rev. C* **89**, 054314 (2014).
63. Goriely, S., Hilaire, S., Girod, M. & Péru, S. First Gogny–Hartree–Fock–Bogoliubov nuclear mass model. *Phys. Rev. Lett.* **102**, 242501 (2009).
64. Baldo, M., Robledo, L. M., Schuck, P. & Viñas, X. New Kohn-Sham density functional based on microscopic nuclear and neutron matter equations of state. *Phys. Rev. C* **87**, 064305 (2013).
65. Pomorski, M. et al. Proton spectroscopy of ^{48}Ni, ^{46}Fe and ^{44}Cr. *Phys. Rev. C* **90**, 014311 (2014).
66. Ascher, P. et al. Direct observation of two protons in the decay of ^{54}Zn. *Phys. Rev. Lett.* **107**, 102502 (2011).
67. Neufcourt, L., Cao, Y., Nazarewicz, W. & Viens, F. Bayesian approach to model-based extrapolation of nuclear observables. *Phys. Rev. C* **98**, 034318 (2018).
68. Kass, R. E. & Raftery, A. E. Bayes factors. *J. Am. Stat. Assoc.* **90**, 773–795 (1995).
69. Kejzlar, V., Neufcourt, L., Maiti, T. & Viens, F. Bayesian averaging of computer models with domain discrepancies: a nuclear physics perspective. Preprint at https://arxiv.org/abs/1904.04793 (2019).

Acknowledgements

We thank the NSCL staff for their technical support as well as R. F. Casten for useful discussions on interpreting the results of the experiment. This work was conducted with the support of Michigan State University, the US National Science Foundation under contracts nos. PHY-1565546 (A.H., E.L., R.J., G.B., K.L., C.R.N., D.P., R.R., C.S.S. and I.T.Y.), PHY-1913554 (R.J.) and PHY-1430152 (R.J.), the US Department of Energy, Office of Science, Office of Nuclear Physics under awards nos. DE-SC0013365 (W.N. and L.N.) and DE-SC0018083 (NUCLEI SciDAC-4 collaboration) (S.A.G. and W.N.) and by the National Science Foundation CSSI programme under award no. 2004601 (BAND collaboration; W.N.).

Author contributions

A.H., E.L., G.B., K.L., C.R.N., D.P., R.R., C.S.S. and I.T.Y. performed the experiment. A.H., E.L., D.P. and I.T.Y. performed the data analysis. A.H., E.L., W.N., S.A.G. and L.N. prepared the manuscript. R.J., S.A.G., W.N. and L.N. performed the Bayesian analysis. All authors discussed the results and provided comments on the manuscript.

Competing interests

The authors declare no competing interests.

Additional information

Correspondence and requests for materials should be addressed to A. Hamaker.

Peer review information *Nature Physics* thanks Alessandro Pastore, Anu Kankainen and Bo Cederwall for their contribution to the peer review of this work.

Reprints and permissions information is available at www.nature.com/reprints.